RESEARCH   **Open Access**

Exploring the synergistic effects of goethite intercalated coal in the presence of humic acids for enhanced growth of *Sinapis alba*

Roza Zharkynbaeva[1], Artur Dzeranov[2,3,4*], Denis Pankratov[5], Daniel Saman[2], Lyubov Bondarenko[2,4], Vera Terekhova[5], Nataliya Tropskaya[2,4], Altynay Mametova[1] and Kamila Kydralieva[2]

Abstract

Background Iron oxide mineral–humic complexes serve as a reservoir of bioavailable Fe for plants, releasing metal ligands and providing Fe–humic complexes directly usable by plant Fe-uptake mechanisms. In this study, we synthesized and characterized goethite α-FeOOH (G) nanoparticles (NPs) intercalated in coal (GC) to estimate the bioactivity effect of humic acids (HA). The synthesized GC NPs were characterized by X-ray diffraction, scanning electron microscopy (SEM), Mössbauer spectroscopy, N_2 adsorption–desorption Brunauer–Emmett–Teller (BET) specific surface area, zeta potential, hydrodynamic particle diameter, iron ions release, and a phytoassay method of root elongation using the higher plant *Sinapis alba*.

Results X-ray diffraction revealed that G was the primary phase in both GC and GC–HA complexes. Mössbauer spectroscopy analysis identified a goethite-doped Fe^{2+}-in the GC samples. The intercalation of G into the coal matrix increased the specific surface area of GC, enhancing its HA sorption capacity. In addition, GC–HA demonstrated superior plant growth stimulation compared to HA and GC alone, indicating its role in colloidal stability. In contrast to GC, GC–HA exhibited a more consistent and time-dependent release of Fe^{3+} and Fe^{2+}. This sustained Fe release from GC–HA, coupled with the formation of Fe^{3+} and more bioavailable (soluble) Fe^{2+} humic complexes is a promising result in terms of iron nanofertilizers production.

Conclusions The use of goethite nanoparticles intercalated within a coal matrix and subsequently complexed with HA contributes to prolonged phytoactivity by employing slowly released nutrient additives within the coal mesoporous matrix.

Keywords Goethite intercalated coal, Humic acids, Higher plants, *Sinapis alba*, Bioactivity effect
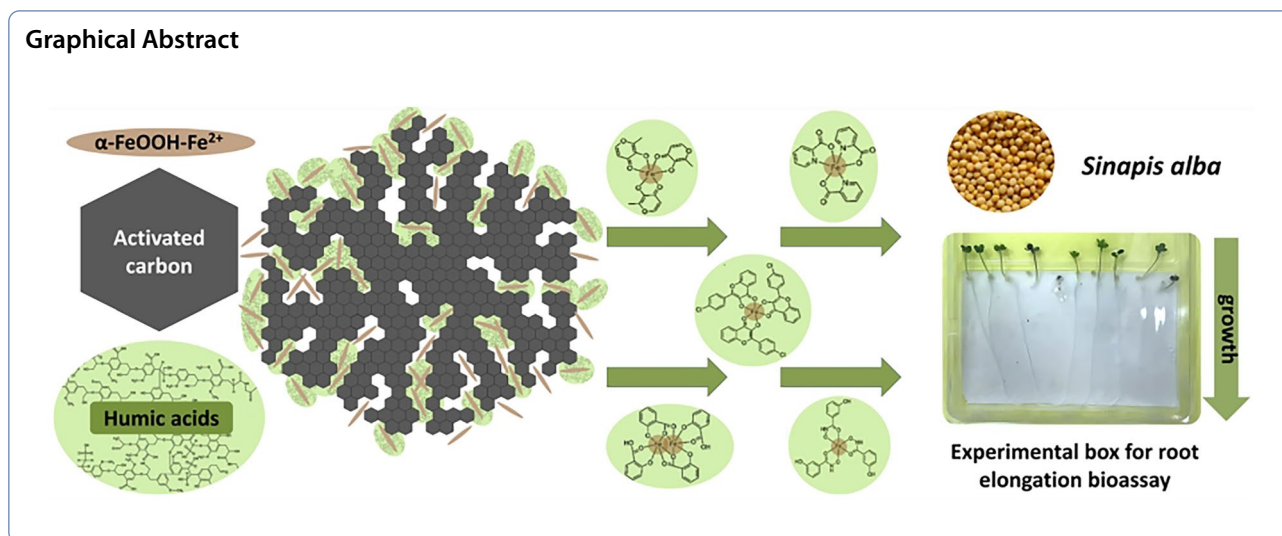
---

*Correspondence:
Artur Dzeranov
arturdzeranov99@gmail.com
Full list of author information is available at the end of the article

Zharkynbaeva *et al. Chem. Biol. Technol. Agric.*   (2024) 11:14

Page 2 of 17

Graphical Abstract

Introduction

Iron (Fe) is an indispensable element for the majority of living organisms, playing a crucial role in cellular respiration, energy conversion, and protein biosynthesis [1]. In agriculture, the development of safe and effective formulations of biologically available iron is of paramount importance.

In the soil environment, iron minerals primarily exist in the form of oxides and hydroxides. Among these iron hydroxides, ferrihydrite $5Fe_2O_3 \cdot 9H_2O$, feroxyhyte δ-FeOOH, lepidocrocite γ-FeOOH, and goethite α-FeOOH exhibit varying thermodynamic stabilities. Goethite stands out as the most thermodynamically stable hydroxide [2] making it a prevalent mineral in soils and sediments. Over time, feroxyhyte can spontaneously transform into goethite, while ferrihydrite can evolve into either hematite [3] or goethite [4].

In the pH range between 7 and 9, the predominant iron mineral forms in the soil are represented by $Fe(OH)_2^+$, $Fe(OH)_3$ and $Fe(OH)_4^-$ hydroxocomplexes. Their concentration in the soil solution is approximately 10^{-10} M. However, for normal plant growth, the concentration of dissolved iron should be several orders of magnitude higher, ranging from 10^{-6} to 10^{-5} M. Iron is an essential micronutrient crucial for various physiological processes in plants, and Fe deficiencies are frequently observed in crops grown in calcareous soils [5]. Iron deficiency causes a plant disease known as iron deficiency chlorosis. To address this issue, soluble iron salts are sometimes applied, but they prove ineffective at low doses and lack long-term efficacy due to Fe ion hydrolysis and subsequent removal from the soluble soil phase through hydroxide precipitation. Alternatively, more effective iron chelates with synthetic organic chelators are used in certain cases

[6]. However, when regularly applied to soil, they accumulate [7], leach into natural waters, and, due to their high complexing ability, contribute to an increase in the mobility and migration of heavy metals and radionuclides in the environment. Using biologically available forms of iron stabilized by humic substances (HS) represents an environmentally friendly method, because HS perform a number of important biospheric functions. These include soil structuring [8, 9], accumulation of nutrients and microelements in a form available to plants [10, 11], and regulation of geochemical fluxes of metals in water and soil ecosystems [12–14]. HS show the ability to form stable complexes with metal ions [15] and to stabilize soil colloids containing oxide nanoparticles [16], while providing a protective effect to organisms under stress [17–19]. Their ability to bind metal ions makes HS suitable for incorporation in the production of microfertilizers and feed and food additives containing trace elements [20]. Furthermore, their redox properties allow the use of HS as reducing agents that limit the mobility of ecotoxicants, such as Cr(VI) [21].

The potential of iron-containing humic preparations as an environmentally safe alternative to synthetic iron chelates was explored in [22]. The study found that iron in humic matrices predominantly exists as highly dispersed hydrated oxides. The effectiveness of iron compounds with HS in alleviating iron deficiency in plants has been consistently demonstrated [23–26]. For example, in the study by [24], nutrient solutions containing iron–humic complexes were used as iron source in plant experiments. The findings indicated that iron–humic complexes serve as a readily absorbable iron source for plants, facilitated by easy uptake by plant roots [25, 26]. The impregnation of mineral oxides offers a novel approach to modifying

Zharkynbaeva *et al. Chem. Biol. Technol. Agric.*   (2024) 11:14

Page 3 of 17

virgin biochar [27] due to the abundance and low cost of iron oxides such as magnetite, maghemite, and goethite [28–30].

This study aimed to develop and characterize goethite nanoparticles intercalated within a coal matrix (GC) and to assess the impact of HA on the biological activity of higher plants, particularly *Sinapis alba (S. alba).* The effect of nanoparticles on plant growth is influenced by various factors, including the type, source, concentration, and size of NPs, the plant species (including developmental stage and growth rate), and the duration of NP exposure to the plants. The size and surface charge of NPs make them potential candidates for plant uptake [5]. The incorporation of HA into formulations containing iron oxyhydroxide nanoparticles intercalated into a coal matrix contributes to a prolonged effect by employing slowly released nutrient additives from the mesoporous coal matrix [31–34]. In addition, this approach appears to enhance bioavailability and environmental friendliness, as these substances naturally form co-precipitates with mineral components (e.g., Fe oxides and clays) or exist in solution, where they significantly contribute to dissolved organic matter.

Materials and methods

Coal treatment

Brown coal from the Min-Kush deposit in the Kyrgyz Republic, designated as "C", was used for both HA extraction and goethite (G) nanoparticle intercalation. Following crushing and screening, the raw coal was sieved and the 1 mm size fraction was retained. To eliminate any impurities from the pores, the G nanoparticles were rinsed with deionized water (DI). They were then homogenized to a size of 50 μm in a high-energy ball mill (SPEX SamplePrep 8000, Mixer/Mill, Tungsten Carbide Vial, Metuchen, NJ, USA) at 1060 rotations per minute (rpm) for 30 min and dried in a centrifugal spray dryer (LPG-5, China) with an inlet air temperature of 210 °C and an outlet air temperature of 105 °C. This treated G was used for both HA extraction and the preparation of GC.

HA extraction procedure from coal

The methodology described by Lowe (1986) with modifications was followed for the extraction of HA from coal. The modifications included pre-homogenizing and grinding the coal to reduce HA extraction time, as well as increasing the extraction temperature as described in [35]. In this study, 20 g of the pre-sieved coal fraction with a particle size of 50 μm was placed in 1 L bottles, and 200 mL of a 1% NaOH solution was added with continuous stirring at 600 rpm. The bottles were sealed with rubber stoppers and equilibrated at 70 °C for 3 h. Following extraction, the dark supernatant was separated

by centrifugation at 1000 rpm for 15 min. Subsequently, 200 mL of 10% HCl solution (approximately pH 2) was added to the supernatant, and the HA was allowed to stand at room temperature for 24 h. The supernatant was then siphoned off from the acidified extracts.

To purify the HA samples, they were washed three times with DI until a nearly neutral pH was achieved. Each washing step involved centrifugation at 10,000 rpm for 10 min. This process effectively removed mineral matter. Following the washing procedure, the purified HA was dialyzed, dried in a centrifugal spray dryer (LPG-50, China) at an inlet air temperature of 105 °C and an outlet air temperature of 50 °C, and stored in a desiccator over P_2O_5.

Goethite intercalated coal preparation

G were synthesized following the method described by Hiemstra et al. [36]. Briefly, 9.8 g of Mohr's salt $((NH_4)_2Fe(SO_4)_2 \cdot 6H_2O)$ was dissolved in 250 mL DI under vigorous stirring at 600 rpm. Subsequently, 50 mL of a 25% NH_4OH solution was added, and the resulting suspension was stirred at 70 °C for 24 h. After this period, the precipitate, G, was thoroughly washed with DI until a neutral pH was attained. Finally, the precipitate was air dried at room temperature for 24 h.

Next, 1.25 g of G and 5 g of C were dispersed in 90 mL of DI. The reaction mixture was stirred at 25 °C for 1 h. Subsequently, the precipitate GC was isolated by centrifugation at 1200 rpm for 30 min. Finally, the precipitate was placed in a desiccator with P_2O_5 until it was completely dry.

GC–HA complex preparation

To prepare a 2 g L^{-1} HA solution, 1 g of HA was dissolved in 450 mL DI, followed by the addition of 50 mL of 10% NaOH. Subsequently, GC–HA complexes were formulated at 1:1 and 1:10 GC:HA (w/w) ratios. The suspensions were gently shaken on a shaker at 150 rpm for 24 h at room temperature without pH adjustment. After the 24-h shaking period, the suspension was centrifuged at 6000 rpm for 15 min. The resulting precipitates were washed three times with DI to remove unbound HA fractions. Following this iterative process, the wash waters were clear and nearly colorless, indicating the successful removal of unbound HA.

Subsequently, the washed precipitates were dried at 60 °C under vacuum conditions. The GC–HA complexes were designated GC–HA1 and GC–HA10, where the index indicates the initial HA concentration (in g L^{-1}) in the complex. Elemental analysis for Fe and carbon for HA showed that the resulting Fe/HA precipitates contained 14% and 6% Fe and 12% and 37% HA, respectively.

Zharkynbaeva *et al. Chem. Biol. Technol. Agric.*   (2024) 11:14

Page 4 of 17

HA content was calculated as a difference between C in GC and C in GC–HA1 and GC–HA10.

Structural characterization of GC and GC–HA

Size and morphology of the samples were observed under a scanning electron microscope (Tescan Vega 3, Czech Republic), and conductive coating (Pt) was applied using magnetron sputtering (Jeol JFC-1600). The coating thickness is no more than 10 nm. The degree of polydispersity was calculated using the modified formula (2.1) derived from Carlos De La Vega's work [37]:

$$K_p = \frac{\partial}{\Delta}, \tag{1}$$

where Kp—degree of polydispersity, ∂—weight average diameter (calculated from the fraction of each particle), Δ—arithmetic average diameter.

X-ray diffraction (XRD) analysis of the nanoparticles was performed using a Philips X-pert Cu-Kα diffractometer ($\lambda = 1.5418$ Å) in the angular range $2\theta = 15–85°$ at a scanning rate of 5 deg min^{-1} and at 25 °C. Diffraction pattern construction and XRD data analysis were performed using Match! and OriginPro software.

Mössbauer absorption spectra for ^{57}Fe were obtained using an Express Mössbauer Spectrometer MS1104EM (CJSC Kordon, Rostov-on-Don, Russia) at temperatures of 296 ± 3 K and 77.7 ± 0.3 K. The γ-radiation source was ^{57}Co in a matrix of metallic rhodium at room temperature. The noise-to-signal ratio for the spectra did not exceed 2%. The mathematical processing of the experimental Mössbauer spectra was performed for high-resolution spectra (1024 points) using the program SpectRelax 2.8 (Lomonosov Moscow State University, Russia). The values of isomer shifts are given relative to α-Fe.

Specific surface area and porous structure analysis of the samples were determined using a Sorptometer-M (Katakon, Russia) at liquid nitrogen temperature (77 K). The Brunauer–Emmett–Teller (BET) and Barrett–Joyner–Halenda (BJH) methods were used to calculate the specific surface area and porous structure characteristics based on the adsorption–desorption isotherms.

To eliminate absorbed gases and vapors from the surface, the samples underwent a "thermal training" process prior to testing. This involved heating them in a stationary nitrogen stream in a vacuum at a temperature of 150 °C.

Surface charging characterization of HA, GC, and GC–HA

The zeta potential of the nanoparticles was determined using electrophoretic light scattering with a NanoBrook Omni particle analyzer. Measurements were performed at a wavelength of 633 nm using a solid-state He–Ne laser, a scattering angle of 173°, and a temperature of 25 °C. Each sample was appropriately diluted in DI to achieve a concentration of 0.1 g L^{-1} for analysis. Consistent time intervals were maintained for all measurements: 10 s of dispersion in an ultrasonic bath followed by an additional 100 s of equilibration. The experiments were performed at 25 ± 0.1 °C in BI-SCP disposable polystyrene plastic cuvettes. Small amounts of 0.1 M HCl or NaOH were added to the suspension to adjust the pH to a range between 2 and 10. pH adjustments were monitored using a pH electrode (Mettler Toledo InLab Expert Pro-ISMO) and a pH meter (SevenExcellence S400).

Elemental analyses (C, H, N, Fe)

Elemental analysis of the samples was performed using an elemental analyzer from Carlo Erba Strumentazione. To determine the ash content, samples were subjected to heating at 800 °C for 4 h. The oxygen content was calculated as the difference between the total mass and the sum of the remaining elements. The H/C and O/C atomic ratios were derived from the elemental contents calculated on an ash-free and moisture-free basis.

Determination of total acidity of HA

Total acidity determination of purified HA was determined following the method described by Inbar et al. [38].

In this procedure, a 5–10 mL aliquot of HA solution containing 5–20 mg HA was transferred to a vial (~22 mL), followed by the addition of 10 mL of 0.03 M Ba(OH)$_2$. The vial was tightly sealed, shaken thoroughly, and allowed to equilibrate for 24 h at room temperature.

After the equilibration, aliquots of the clear solution above the barium humate precipitate were transferred to a titration cell and titrated with a standard HCl solution (0.1 M) using phenolphthalein as an indicator. The total acidity (TA, mmol g^{-1}) was calculated according to formula (2):

$$TA = \frac{(V_0 - V_{HA}) \cdot C_{HCl}}{m}, \tag{2}$$

where V_0 and V_{HA} are the volumes of HCl consumed for the blank and sample titrations (mL), respectively, C_{HCl} is the titrant concentration (mmol mL^{-1}), and m is the mass (g) of HA in the aliquot.

A saturated Ba(OH)$_2$ solution was carefully prepared by dissolving BaO in CO$_2$-free DI (boiled for 1 h) in a sealed volumetric flask with vigorous shaking. The solution was allowed to stand for 3–4 days until complete precipitation of BaCO$_3$ occurred. Working solutions were freshly prepared just before analysis by diluting an aliquot of the transparent supernatant and standardizing against HCl.

Determination of carboxylic acidity of HA

The Ca acetate method, as described by [39], was used to determine the content of strong acid groups in the humic samples. In this method, a 5–10 mL aliquot of HA solution containing 5–20 mg HA was transferred to a vial (22 mL), followed by the addition of 10 mL of 0.6 M $Ca(CH_3COO)_2$. The vial was tightly sealed, shaken thoroughly, and allowed to equilibrate for 24 h at room temperature.

After equilibration, aliquots of the clear solution above the precipitate of Ca-humates were transferred to a titration cell and titrated with a standard NaOH solution (0.05 M) using an autotitrator. The carboxyl acidity (CA, mmol g^{-1}) was calculated according to formula (3):

$$CA = \frac{(V_{HA} - V_0) \cdot C_{NaOH}}{m},$$ (3)

where V_0 and V_{HA} are the volumes of NaOH consumed for the blank and sample titrations (mL), respectively, C_{NaOH} is the titrant concentration (mmol mL^{-1}), and m is the mass (g) of HA in the aliquot.

Size exclusion chromatography (SEC) of HA

SEC analysis was performed according to [40] using a column (25 mm × 20 cm) packed with Toyopearl HW-50S gel (Toso Haas, Japan). Polydextrans were used as markers for molecular weight calculations. Prior to analysis, HA solutions were adjusted to a concentration of 1–2 mg C L^{-1} by equilibration with the SEC mobile phase (0.028 M phosphate buffer, pH 6.8). The flow rate was set at 1 mL min^{-1}, and the absorbance of the eluate was monitored at 254 nm. Peak molecular weight (Mp) is the molecular weight at the peak of the distribution curve.

Number average molecular weight (Mn) is defined by formula (4):

$$\overline{M_n} = \frac{\sum n_i M_i}{\sum n_i},$$ (4)

where n_i is number of *i*th molecules with molecular weight M_i.

The weight average molecular weight is calculated according to the following Eq. (5):

$$\overline{M_w} = \frac{\sum N_i M_i^2}{\sum n_i}.$$ (5)

Characterization of the HA

Information on the elemental composition, carboxylic and phenolic group content, and molecular weight distribution of HAs is summarized in Tables 1 and 2.

Detection of Fe ions release

The mass concentration of released Fe^{3+} and Fe^{2+} ions was determined following the methods with modification described in [41, 42]. GC and GC–HA powders were suspended in 0.1 M sodium acetate buffer (pH = 4.6, 0.6% NaCl) and subjected to centrifugation (6000 rpm, 5 min) at intervals of 0, 0.5, 1, 3, and 24 h. After separation, specific ion detection reagents were added to the supernatant.

For Fe^{3+} ions detection, 200 μL of potassium thiocyanate (KSCN) (50% solution) and 200 μL of HCl (18.25% solution) were added to 5 mL of the supernatant, initiating a reaction under strongly acidic conditions with a pH close to 2. The solution was allowed to equilibrate for 20 min, and the absorption spectrum was measured at 480 nm.

For Fe^{2+} ions detection, 2 mL phenanthroline ($C_{12}H_8N_2$-H_2O) (2.5% solution) and 600 μL of sodium acetate were added to 5 mL of the supernatant. Similarly, the solution was allowed to equilibrate (with no observable color change) for 20 min and inspected at 510 nm.

Absorbance measurements were performed using a UV–Vis–NIR spectrophotometer (Cary UV–Vis–NIR Spectrophotometer, Agilent Technologies).

Table 2 Peak molecular weight Mp, number average molecular weight Mn, weight average molecular weight Mw, and polydispersity Mw/Mn of HA

Mp, kDa	Mn, kDa	Mw, kDa	Mw/Mn
8.6	1.6	8.3	5.2

Table 1 Elemental, carboxylic, and phenolic group composition of HA

Elemental content on ash and moisture-free basis, %				Ash, %	Atomic ratios		Carboxylic and phenolic group content, mmol g^{-1}		
C	H	N	O		H/C	O/C	COOH	Phenolic OH	Total acidity
62.2	4.4	0.85	32.12	6.12	0.85	0.39	4.6	1.3	5.9

Zharkynbaeva *et al. Chem. Biol. Technol. Agric.*   (2024) 11:14

Page 6 of 17

Phytoassay method

The root elongation phytoassay method, widely used for quality assessment of metal-bearing samples, is based on various protocols (US EPA, 1996; ISO 11269-1, 2012) [43, 44]. This method is favored due to its cost effectiveness, simplicity, and short duration [43].

In this study, white mustard (*Sinapis alba* L.) was selected for the phytoassay to investigate the dose–response relationship of aqueous suspensions of iron-based nanoparticles in a 96-h root elongation phytoassay test, in accordance with the recommendations of ISO 18763:2016 and the Russian standard method (Russian Federal Register FR 1.31.2012.11560) [44].

The experimental setup comprised specially designed boxes, each containing two compartments measuring $13.5 \times 8.5 \times 0.8$ cm (length x width x height), corresponding to a volume of 92 cm^3 per compartment. The lower compartment, designated for root growth, was filled with filter paper soaked in an aqueous suspension of nanoparticles, while the upper compartment accommodated shoot growth.

The filter paper in the lower compartment was evenly moistened with 10 mL of the aqueous nanoparticle suspension. Subsequently, ten *Sinapis alba* L. seeds were placed on the filter paper. The test boxes were sealed with a transparent lid and initially incubated horizontally at 20 ± 2 °C in the dark for 24 h, followed by 72 h in a vertical position at 24 ± 2 °C under illumination for 16 h per day, maintaining a light intensity of 4000–7000 lx (light wavelength 400–700 nm, universal white).

At the conclusion of the incubation period, the length of the main root of the mustard seedlings was measured and the mean value was calculated and compared to the control values. The assay was performed in triplicate.

Statistics

The phytoassay effect of tested dilutions compared to the control was calculated as a percentage (%). Statistical processing of phytoassay results was performed using one-way ANOVA; p-values were calculated using the Statistica 10 statistical package (StatSoft Inc., USA).

Results

X-ray diffractograms, SEM observation, and Mössbauer spectra of GC, GC–HA1, and GC–HA10

The X-ray diffractograms of GC, GC–HA1, and GC–HA10 exhibit narrow and symmetrical peaks, indicating the presence of crystalline material (Fig. 1). The noise-to-signal ratio was relatively high due to the carbon matrix. The primary structural parameters of the nanoparticles were determined and are summarized
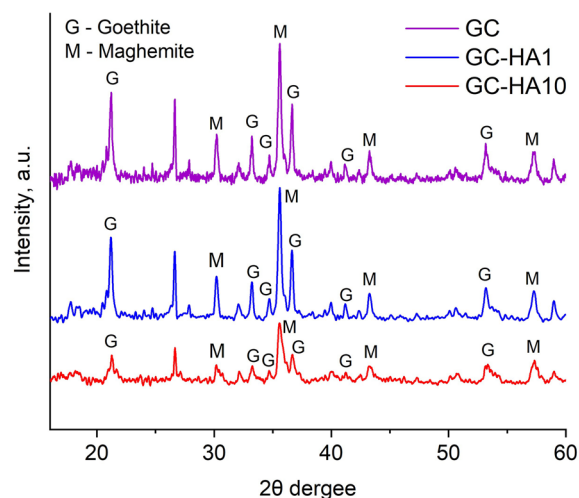

Fig. 1 XRD data of GC, GC–HA1, and GC–HA10 samples

Table 3 Quantitative evaluation of XRD data by the Rietveld method and SEM data for GC, GC–HA1, and GC–HA10

Sample	GC	GC–HA1	GC–HA10
Main phase	goethite	goethite	goethite
a, Å	4.456	4.448	4.436
b, Å	10.207	10.112	9.912
c, Å	2.992	2.989	2.980
D_{XRD}, nm	21 ± 4	25 ± 3	37 ± 9
D_{SEM}, nm	65.48 ± 12.10	66.68 ± 17.88	112.16 ± 15.32
Kp	0.95	0.97	0.98
CV,%	26.6	18.3	13.6

in Table 1. The phase states of the nanoparticles were determined using the Crystallography Open Database.

Table 3 presents a quantitative analysis of the XRD data, with a focus on the unit cell parameters determined by the Rietveld method. The primary phase identified in the synthesized NP samples matches the predicted goethite α-FeOOH phase, corroborating the available data [45]. In addition, reflections corresponding to maghemite impurity were detected [46]. The introduction of HA did not alter the goethite phase; maghemite also remained present. Slight variations in the average nanoparticle sizes were observed upon the addition of a high concentration of HA (10 wt.%). The sizes of the coherent scattering regions were 21 ± 4, 25 ± 3, and 37 ± 9 nm for GC, GC–HA1, and GC–HA10 NPs, respectively.

The size of the coherent scattering region was determined using the Scherrer method based on powder XRD data. Changes in nanoparticle size due to coating were investigated by SEM and XRD analysis, showing a correlation between the two techniques. Despite maintaining a
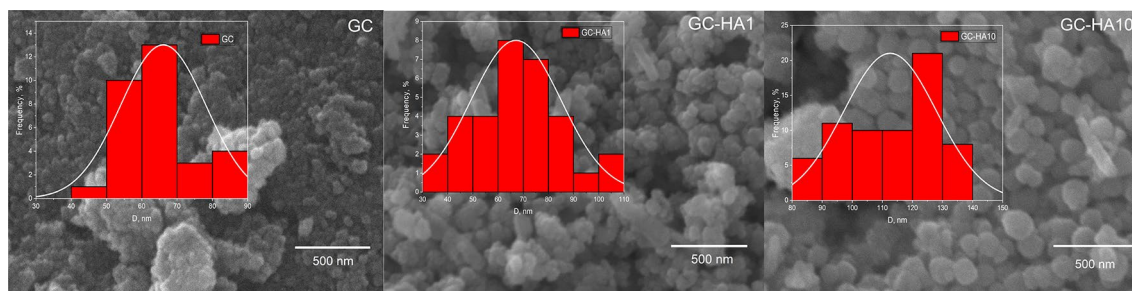
Zharkynbaeva *et al. Chem. Biol. Technol. Agric.*   (2024) 11:14

Page 7 of 17

Fig. 2 SEM images of GC, GC–HA1, and GC–HA10

consistent spherical particle shape across all modification routes, subtle particle growth was observed (Fig. 2).

The bare GC particles had an average particle diameter of 21.0 nm and 65.5 nm according to XRD and SEM analyses, respectively. Following modification, the GC–HA1 particles exhibited an increase in size to 25.0 nm (XRD) and 66.7 nm (SEM) compared to bare GC. Notably, the GC–HA10 particles exhibited a more substantial increase in diameter to 37.0 nm (XRD) and 112.1 nm (SEM) compared to bare GC.

The larger crystallite size observed in HA-modified NPs compared to bare GC was attributed to the higher concentration of HA. Moreover, the addition of 10% HA induced particle structuring or an increased degree of crystallinity, characterized by a more pronounced contour and a strictly spherical shape, as evident in the SEM images. On the other side, supramolecular associates of HA, self-assembled due to hydrophobic interactions and hydrogen bonds of numerous low-molecular components [47, 48], are also fractioned since the external forces from mineral surfaces on some small molecules exceed the intermolecular forces between the molecular components of HA [49]. As a result, the well-ordered structures of crystalline are observed for GC–HA1 and GC–HA10.

Based on the coefficient of variation (CV) and polydispersity index (Kp) values obtained from the SEM analysis, it is noteworthy that GC–HA10 has a narrow size distribution (13.6%, 0.98) compared to GC (26.6%, 0.95) and GC–HA1 (18.3%, 0.97). Although all samples fall under the polydisperse category according to [37], the CV of 13.6% and Kp of 0.98 for GC–HA10 indicate a higher degree of homogeneity in the nanoparticles. This homogeneity is essential for achieving optimal performance in the final surface-activated material.

The addition of HA had a moderate effect on particle size but also influenced the lattice parameters of GS, as evidenced by XRD and Mössbauer spectroscopy.

Relying solely on XRD for identifying the crystal structure of iron (oxyhydr)oxides is insufficient because a significant portion of the material might be X-ray amorphous. Therefore, Mössbauer spectroscopy was used to complement the structural analysis of iron (oxyhydr)oxides. Given the remarkable similarity in XRD patterns for GC and GC–HA1, regardless of HA addition, Mössbauer spectral analysis was exclusively performed for GC and GC–HA10 samples.

The experimental Mössbauer spectra acquired at 296 K for GC and GC–HA10 samples exhibit a complex array of more than a dozen resonance lines with varying intensity, width, and profile (Fig. 3), indicating the intricate composition of the studied materials. The distortion in the profile of the resonance lines of the sextets towards the inner part of the spectrum reveals the small size of the corresponding magnetic domains, a characteristic feature of nanoscale materials.

These circumstances contribute to the complexity of describing the Mössbauer spectra model. A satisfactory mathematical description of the spectral profile could only be achieved by employing a superposition of two symmetric doublets and two nested sextets, each characterized by different probability distribution functions for hyperfine parameters (Table 2). Specifically, for the inner sextet, only the distribution probability of the hyperfine magnetic field was considered, while for the outer sextet, the probabilities of changes in both the magnetic field and the isomer shift were considered, and these were linked to the same distribution function (Table 2).

The probability distribution function for the inner sextet's magnetic field exhibits a unimodal, highly dispersed, and asymmetric profile due to a substantial broadening towards the low-field region (Fig. 3). The hyperfine parameters obtained for this sextet conclusively assign it to goethite [50, 51].

Examination of the probability distribution function profiles for the outer sextet's isomer shift and magnetic field reveals two distinct modes. These modes correspond to iron atoms in octahedral (large isomer shift and smaller magnetic splitting—Table 4) and tetrahedral (smaller isomer shift and larger magnetic splitting) sites of non-stoichiometric magnetite—$Fe_{3-\delta}O_4$ [52, 53]. The

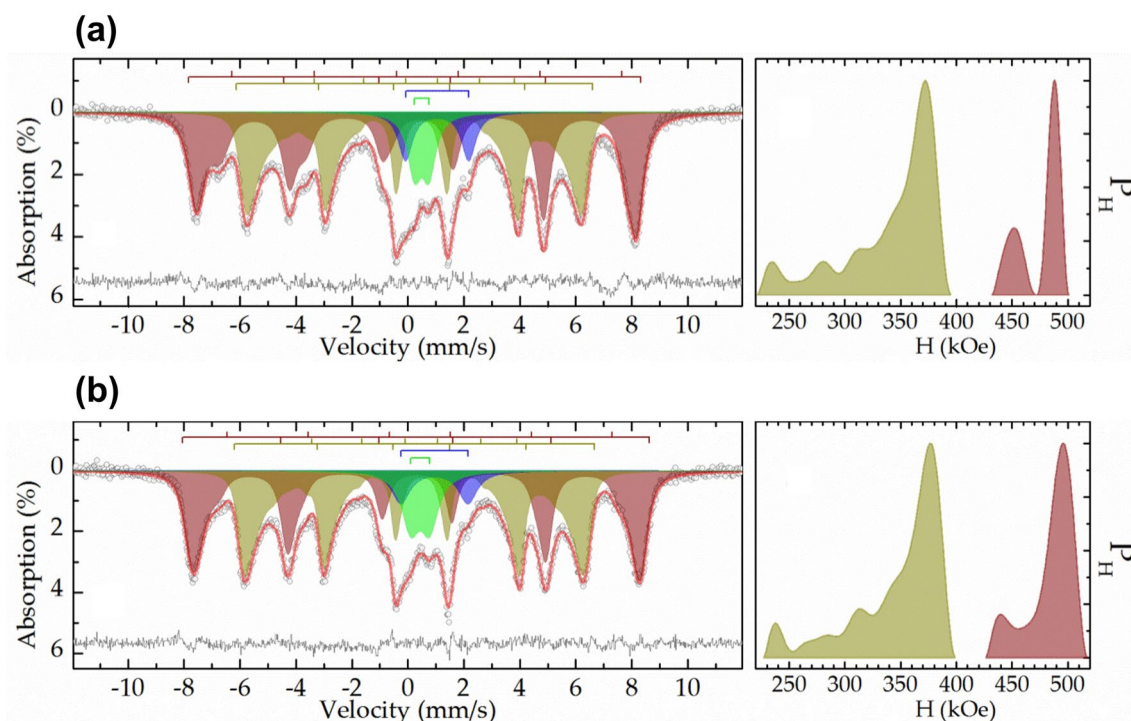Zharkynbaeva *et al. Chem. Biol. Technol. Agric.*   (2024) 11:14

Page 8 of 17

Fig. 3 Experimental Mössbauer spectra obtained at 296 K, as well as models for their description and probability distribution functions of hyperfine magnetic fields for GC (**a**) and GC–HA10 (**b**) samples

hyperfine parameters of the doublets responsible for the absorption in the central part of the spectra correspond to $+2$ and $+3$ oxidation state iron atoms (Table 2, sub-spectrum 3 and 4, respectively) in octahedral oxygen sites [54].

Comparing the high-temperature spectra of the samples, a noticeable broadening of the doublets responsible for the paramagnetic part of the spectrum is observed for GC–HA10 compared to GC. This broadening may indicate a degree of disorder in the corresponding crystalline fragments. In addition, the modes on the profile of the probability distribution function of the magnetite sub-spectrum for the GC–HA10 sample exhibit substantial dispersion and are poorly resolved. This could be attributed to the partial oxidation of the magnetite phase in the GC–HA10 sample by HA [55, 56].

Upon cooling the samples to liquid nitrogen temperature, the Mössbauer spectra undergo a remarkable transformation: a sextet, albeit distorted, becomes clearly visible, and the intensity of the spectra increases approximately twofold (Fig. 4). For both samples, a satisfactory description of the experimental spectra is achieved by using a superposition of two symmetric doublets, similar to those described for the high-temperature spectra, and a sextet characterized by the

probability distribution function of the quadrupole displacement and the hyperfine magnetic field (Table 2). This function comprises two modes with a regular symmetric profile, presumably corresponding to two iron-containing phases (Fig. 4).

The more intense mode, characterized by substantial quadrupole shift and minimal hyperfine magnetic field, is attributed to the goethite phase [50, 51]. The second, less intense mode, exhibiting a quadrupole shift close to zero and a high hyperfine magnetic field, reflects the state of the iron atoms in non-stoichiometric magnetite. Based on the relative intensity of the corresponding mode, the magnetite content in the material is estimated to be 20–30%.

Therefore, Mössbauer spectroscopy revealed that the investigated samples are predominantly composed of goethite, with non-stoichiometric magnetite identified as the primary impurity.

The Mössbauer spectra of GC–HA10 corroborate that iron in the nodules primarily resides in the ferric oxyhydroxide form, constituting a goethite doped with Fe^{2+}. HA are known to exhibit redox reactivity and the ability to chemically reduce metals, including Fe^{3+} [57, 58]. Studies have demonstrated that both dissolved and solid-phase HA can accelerate the reduction of Fe(III) oxide in sediments [59, 60] and facilitate the

Table 4 Mössbauer spectra parameters for GC and GC–HA10 samples

Temperature, K			296 ± 3					77.7 ± 0.3				
Sample	No.	Site	$\delta\,(\delta_{ext})$ * mm s^{-1}	$\varepsilon\,\{\Delta=2\varepsilon\}$	Γ_{exp}	H_{ext} kOe	S %	δ mm s^{-1}	$(\varepsilon_{ext})\,\{\Delta=2\varepsilon\}$	Γ_{exp}	H_{ext} kOe	S %
GC	1	$Fe_{3-\delta}O_4$	(0.32 ± 0.01) (0.56 ± 0.02)	0.00 ± 0.01	0.57 ± 0.01	488.3 ± 0.6 452 ± 4	43.0 ± 0.3	0.47 ± 0.01	(−0.02 ± 0.01)	0.40 ± 0.01	525 ± 1	85.5 ± 0.2
	2	GC	0.36 ± 0.01	− 0.13 ± 0.01	0.34 ± 0.01	372.3 ± 0.9	42.2 ± 0.3		(−0.10 ± 0.01)	0.49 ± 0.03	497.2 ± 0.4	6.0 ± 0.3
	3	Fe^{+2}_{Oh}	1.05 ± 0.01	{2.26 ± 0.01}	0.62 ± 0.02		6.9 ± 0.2	1.32 ± 0.01	{2.26 ± 0.02}	0.98 ± 0.07		8.5 ± 0.4
	4	Fe^{+3}_{Oh}	0.50 ± 0.01	{0.51 ± 0.01}	0.60 ± 0.02		8.0 ± 0.2	0.48 ± 0.02	{0.94 ± 0.04}			
GC–HA10	1	$Fe_{3-\delta}O_4$	(0.32 ± 0.01) (0.41 ± 0.01)	0.00 ± 0.01	0.47 ± 0.01	496.1 ± 0.7 440 ± 2	39.2 ± 0.3	0.47 ± 0.01	(− 0.01 ± 0.01)	0.40 ± 0.01	526 ± 1	87.3 ± 0.3
	2	GC	0.36 ± 0.01	− 0.13 ± 0.01	0.33 ± 0.01	376.9 ± 0.6	43.1 ± 0.4		(− 0.10 ± 0.01)	0.41 ± 0.04	498.1 ± 0.7	3.0 ± 0.3
	3	Fe^{+2}_{Oh}	0.95 ± 0.01	{2.39 ± 0.02}	0.89 ± 0.04		7.2 ± 0.3	1.32 ± 0.01	{2.34 ± 0.03}	1.28 ± 0.09		9.7 ± 0.4
	4	Fe^{+3}_{Oh}	0.44 ± 0.01	{0.69 ± 0.01}	0.79 ± 0.03		10.5 ± 0.3	0.51 ± 0.02	{1.07 ± 0.05}			

* δ – isomeric shift, ε – quadrupole shift, $\{\Delta=2\varepsilon\}$ – quadrupole splitting, Γ_{exp} – linewidth, H – hyperfine magnetic field, S – relative subspectrum area, (F_{ext}) – the value of the parameter F at the extremal point of the probability density function
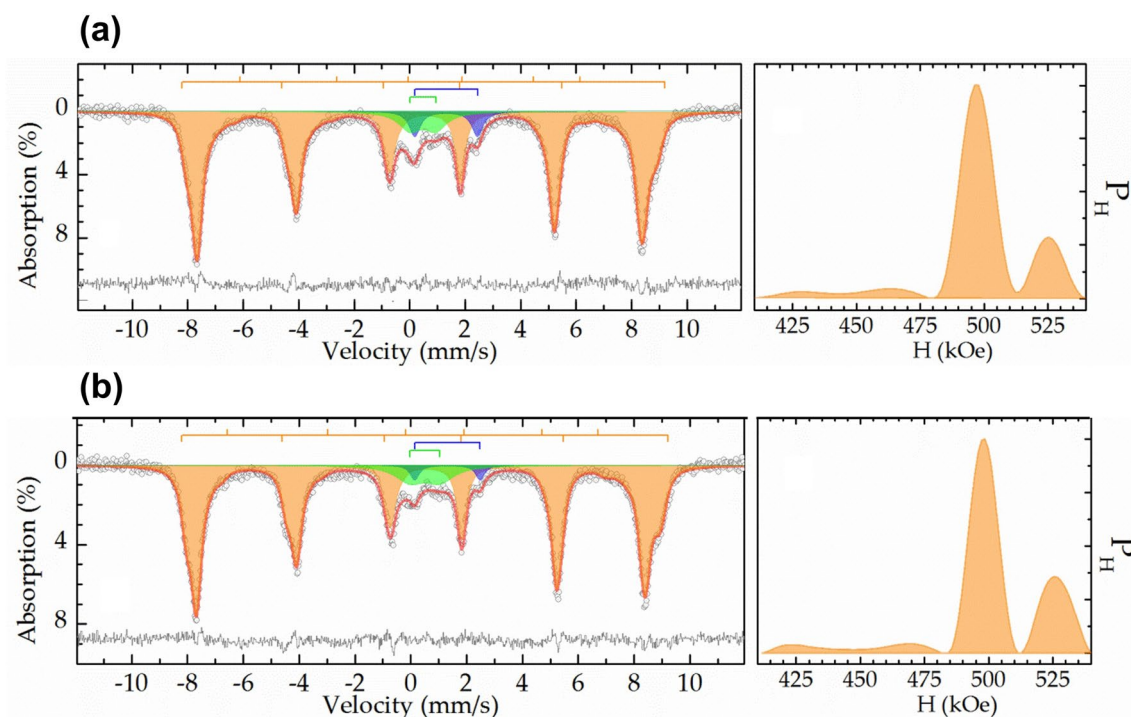
Fig. 4 Experimental Mössbauer spectra obtained at 78 K, as well as models for their description and probability distribution functions of hyperfine magnetic fields for GC (**a**) and GC–HA10 (**b**) samples
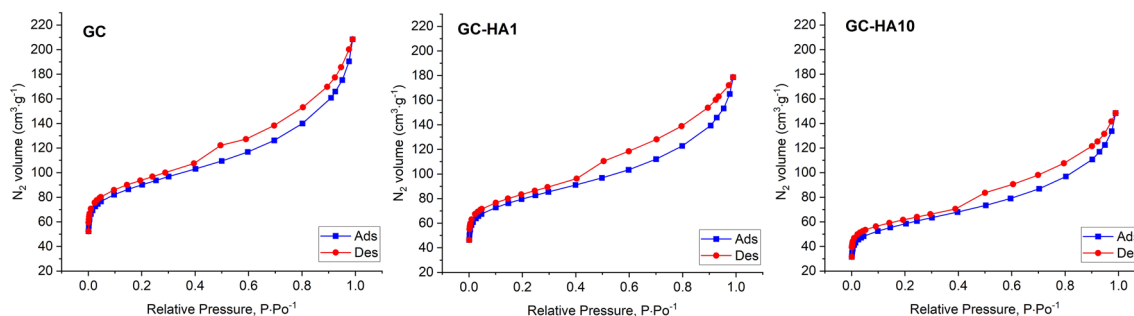

Fig. 5 Isotherms of nitrogen adsorption/desorption of samples at low temperature (77 K)

bioreduction of Fe(III) minerals in soils [61] by acting as electron shuttles between bacteria and oxide surfaces.

Textural characteristics of GC, GC–HA1, and GC–HA10

Figure 5 presents the N_2 adsorption/desorption isotherms for nanoparticles. The samples exhibit type IV isotherms, characteristic of polymolecular adsorption and the presence of capillary condensation in mesopores. The isotherms show H4 type hysteresis loops, characterized by a pronounced steep rise at low pressures, indicative of micropores.

Table 5 Textural characteristics of GC, GC–HA1, and GC–HA10

Sample	BET		BJH	
	SSA, m^2 g^{-1}	Pore volume, cm^3 g^{-1}	Pore volume, cm^3 g^{-1}	Pore diameter, nm
GC	328.3	0.32	0.21	3.60
GC–HA1	289.5	0.28	0.18	3.67
GC–HA10	210.5	0.23	0.16	3.60

The results of the BET method for specific surface area (SSA) and the BJH method for average pore diameter are presented in Table 5. The data consistently show a decrease in SSA from 289.5 to 210.5 m^2 g^{-1} and a decrease in BET pore volume from 0.28 to 0.23 cm^3 g^{-1}. This suggests that higher HA concentrations during sorption lead to the blocking of more micropores. Interestingly, the pore diameter remains unchanged, probably due to the absence of HA adsorption on the pore walls, possibly attributed to the negative charge on the inner surface of the pores.

Zeta potential and hydrodynamic diameter of HA, GC, GC–HA1, and GC–HA10 as a function of pH

Zeta potential measurements provide valuable insights into the surface electrical properties of materials. The pH-dependent surface charging behavior of iron (oxy-hydr)oxides, which significantly influences their affinity for anions and cations, is well documented in the literature [62]. Figure 6 illustrates the pH-dependent variations in zeta potential and hydrodynamic particle diameter for HA and GC, considering GC both in its individual state and when combined with HA.

With increasing pH, the dissociation of surface OH groups induces surface recharging, resulting in a consequential increase in the negative charge of iron nanoparticles:

$$= Fe - OH(surf) + OH^- \leftrightarrow = Fe - OH^- + H_2O$$

The isoelectric point of GC in the absence of HA is observed at a pH (pH_{IEP}) of approximately 5.5, which is lower than most reported values for pristine goethite [62] owing to the influence of the carbon matrix. At pH values below 5.5, the GC surface is positively charged, transitioning to negative at higher pH values.

The speciation of HA in solution depends on ionic strength and pH. Initially, with increasing pH, carboxylic groups dissociate protons. Around neutral pH, a significant portion of these carboxylic groups have already dissociated, prompting the gradual dissociation of phenolic hydroxyls [63].

In the presence of HA, a noticeable shift in the pH isoelectric point is observed, from 5.3 for initial particles to 4 and 3.2 for 1 and 10 wt/wt GC–HA, respectively. This shift is consistent with classical specific adsorption of anions (in this case, HA polyanions), resulting in a lower pH_{IEP}.

The reduction in negative charges on the G surface in the presence of 10 wt% HA polyanions can be attributed to the conformational structure of the polyelectrolytes [64]. At higher concentrations of polyelectrolytes, there is a tendency towards a twisted structure, exposing fewer COOH/OH ions on the HA surface [64].

The decrease in zeta potential observed in the pH range 4.5–8 for the GC–HA10 sample suggests an aggregation process, further supporting the change in HA conformation with increasing concentration.

The hydrodynamic particle diameter of the samples was determined at pH 6.5 in DI, corresponding to phytoassay conditions. Under these conditions, electrostatic repulsive interactions between HA molecular segments contribute to an apparent increase in the average hydrodynamic diameter, reaching 460 nm at pH 6.5 [65].

The average hydrodynamic particle size for GC remained relatively unchanged after modification with 1 wt% HA, measuring approximately 300 nm for both samples. However, increasing the concentration of HA in GC to 10 wt% induced particle flocculation, resulting in a reduction in hydrodynamic diameter to about 150 nm. This phenomenon can be attributed to an enhanced
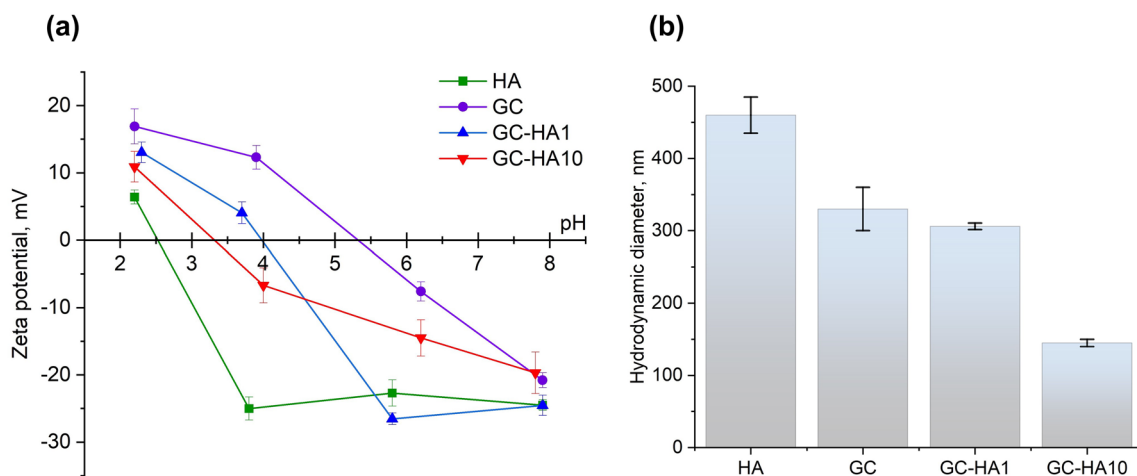

Fig. 6 a Zeta potential (mV) vs pH and **b** hydrodynamic particle diameter (nm) at pH 6.5 for HA, and for GC with and without HA
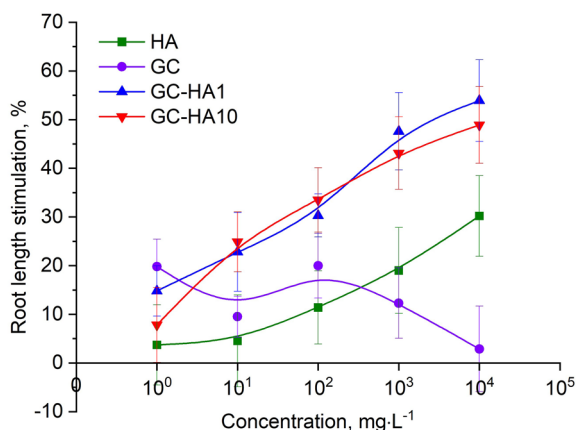
Fig. 7 Dose–effect relationship of plants root length for different samples. All concentrations are nominal. Average values±SD of in triplicates are shown

charge neutralization process arising from the excess fraction of protonated OH groups of HA ($pKi_2 \sim 9$ [66–68]), which do not directly participate in the coordination with G [69].

Phytoassay

The biological activity of iron nanoparticles was evaluated using the plant (*S. alba*) root elongation method, with the results presented in Fig. 7. The suspensions were maintained within the biologically and environmentally relevant pH range of 6–7. Statistical analysis using one-way ANOVA revealed a highly significant difference between the mean values of the groups (p-value < < 0.05).

The phytoassay revealed a subtle, wave-like stimulation of plant root elongation upon application of GC preparation at low concentrations ($10–10^2$ mg L^{-1}). However, increasing the GC concentration to 104 mg L^{-1} resulted in a decrease length of plant root. These results are consistent with previous studies [70] that have demonstrated diverse bioeffects, including responses under stress conditions. In addition, our study highlighted the concentration-dependent toxic effects of iron oxide nanoparticles attributed to oxidative stress [70].

HA, known for their plant growth-promoting properties [19, 71], consistently exhibited a stimulatory effect on root length growth, reaching up to 30% compared to the control.

The highest root length stimulation was observed for GC–HA1 and GC–HA10 compared to HA and GC alone. Notably, despite an order of magnitude increase in the concentration of HA in these samples, no change in bioactivity was observed. This suggests that the enhanced stimulation of mustard root growth by hybrid complexes GC–HA1 and GC–HA10 compared to HA and GC alone is likely due to the influence of Fe ions, including their presence as part of water-soluble complexes with HA. To validate this proposed mechanism, UV–Vis spectroscopy was used to investigate the kinetics and concentration of Fe^{2+} and Fe^{3+} released from the samples.

Release of Fe ions

UV–Vis spectroscopy was used to investigate the kinetics and concentration of Fe^{2+} and Fe^{3+} released from the samples (Fig. 8). Considering that the phytoassay results were evaluated after 96 h at pH ~ 6.5, the release of Fe^{2+} and Fe^{3+} within the same 96-h time frame at the
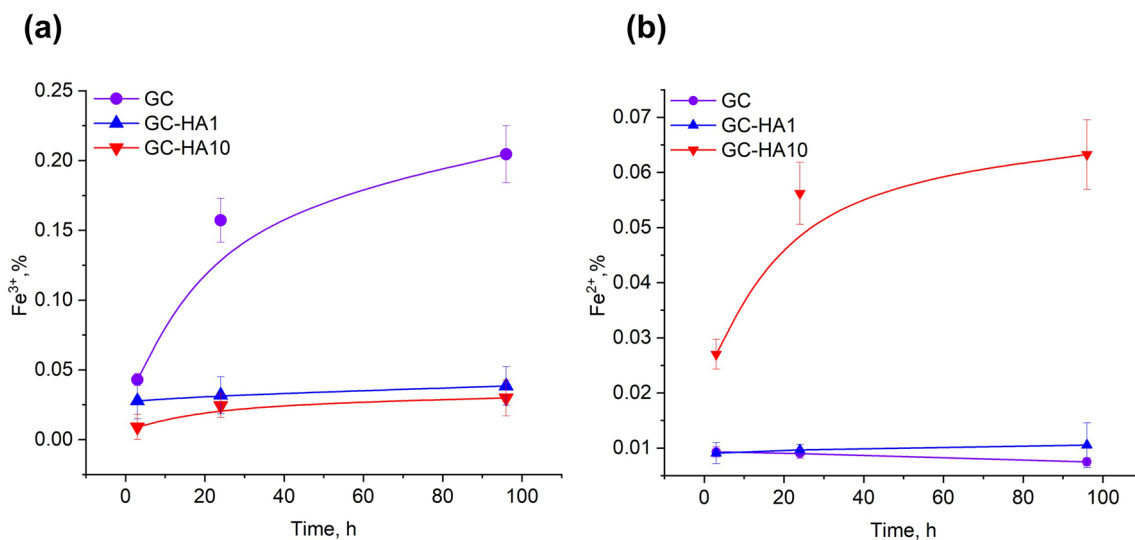

Fig. 8 **a** Fe^{3+} and **b** Fe^{3+} ion release kinetics from GC with and without HA (1 and 10 g L.$^{-1}$ initial concentration)

specified pH was determined. Mössbauer spectroscopy data corroborated the presence of Fe^{2+} in the samples. The concentrations of iron ions per gram of sample were recalculated.

Complexometric titrations with potassium rhodanide for Fe^{3+} and potassium o-phenanthroline for Fe^{2+} (Fig. 8) revealed that both GC and HA-modified complexes release both Fe^{2+} and Fe^{3+}. However, the concentration of ions released by the samples varies. GC nanoparticles released the highest concentration of Fe^{3+} and Fe^{2+} compared to those modified by HA. This dissolution of iron oxide nanoparticles is a well-documented phenomenon [72].

The kinetics of total ion release varied across all samples. Notably, the GC sample exhibited continuous dissolution over time, failing to reach equilibrium within 96 h. A rapid initial release of Fe^{3+} and Fe^{2+} from the GC sample was observed within the first hour, followed by a sharp decrease in concentration. This observation suggests a possible reverse sorption of ions or the formation of iron hydroxides [73, 74].

The GC–HA1 and GC–HA10 complexes exhibited a sustained, low-level release of Fe^{3+} and Fe^{2+} over 96 h. The slightly reduced detectable release of Fe^{3+} and Fe^{2+} ions for the GC–HA10 sample is likely attributable to the formation of multiple surface bonds of COOH groups of HA and the OH groups of the GC surface via ligand exchange [75].

The dissolution rate of the studied samples also bears a proportional relationship to the particle surface area. This observation aligns with the Noyes–Whitney equation [76] and the Ostwald–Freundlich equation [77], both of which suggest that smaller nanoparticles dissolve more rapidly than larger ones.

Discussion

The XRD analysis results indicated that the crystal structure of GC–HA complexes did not exhibit significant alterations with increasing HA content compared to GC. However, the peak intensity of the complexes decreased, and the average nanoparticle size increased for GC–HA10. Mössbauer spectroscopy revealed the presence of Fe^{2+} following the modification of GC with HA. The reduction of Fe^{3+} occurred due to the well-known redox properties of HA [57, 58].

In this study, Fe^{3+} and Fe^{2+} release was detected using the complexometric method to estimate Fe mobilization into the aqueous solution at neutral pH. The most abundant Fe^{3+} species in the environment has low bioavailability [78] compared to the Fe^{2+} form, which has better solubility under certain conditions and can be more easily absorbed by plants [79].

The observed reduction in hydrodynamic diameter and zeta potential in aqueous suspension of GC–HA10, determined by DLS and EDS methods, can be attributed to conformational changes in HA as previously documented in the literature [64]. Importantly, this change in properties results in a bioactivity effect comparable to that observed with GC–HA1.

Moreover, the intercalation of G into the coal matrix resulted in a significant increase in the surface area of GC. The specific surface area of G, as measured by the BET N_2 method, is reported to be 94 $m^2 \, g^{-1}$ [80]. While the modification of GC with 10 wt% HA resulted in a decrease in surface area from 328.3 $m^2 \, g^{-1}$ to 210.5 $m^2 \, g^{-1}$, it is noteworthy that the specific surface area of GC–HA remained higher than that of G-NPs alone. Weng et al.) [80] has previously calculated that the surface sites of G that form chemical bonds with HA are generally small. The adsorption of HA on these surface sites may physically block them, potentially limiting the formation of surface complexes between small ions and oxides [80]. Crucially, the increased surface area resulting from the intercalation of G into the coal matrix was identified as a key factor contributing to the increased adsorption of HA. Consequently, the increase in specific surface area achieved by using coal as a matrix for G intercalation defines the extended surface sites and consequently the reactive behavior of GC–HA in this study.

The bioactivity of hybrid complexes containing iron oxides in a coal matrix, along with HA, is governed by intricate mechanisms that can vary depending on specific environmental conditions. In our model experiments, we evaluated the influence of Fe mobility on plant growth by measuring the release of Fe ions from the studied samples GC–HA1 and GC–HA10 using the complexometric method. However, the low percentages of Fe^{3+} and Fe^{2+} determined in our study likely resulted from the use of different extraction conditions compared to the real conditions encountered by seeds during germination. Specifically, we employed potassium thiocyanate for Fe^{3+} and potassium o-phenanthroline for Fe^{2+} in distilled water, whereas actual root exudates contain organic acids capable of desorbing iron from humic complexes. These organic acids possess high stability constants for iron complexes [81–83], enabling them to effectively displace the metal from the chelating centers of HS. Therefore, the extraction capacity of potassium thiocyanate and potassium o-phenanthroline may be significantly lower than that of the root exudates in natural environments.

Previous studies, including our own [84], have demonstrated that Fe ions at certain concentrations can trigger the Fenton reaction, leading to oxidative stress and plant growth inhibition. Both extracellular and intracellular reactive oxygen species (ROS) can be

generated by iron-based NPs, with the former activating the latter [85]. Elevated ROS levels induce oxidative damage and toxicity, as evidenced by increased malondialdehyde levels and reduced catalase and glutathione expression. The effects of ROS on superoxide dismutase activity vary across different studies [86–88]. Recently, Chaithawiwat et al. [89] demonstrated that *E. coli* mutants lacking oxidative stress defense genes were more susceptible to nano-zero valent iron (nZVI) than the wild type, highlighting the crucial role of ROS-mediated oxidative stress in the toxicity mechanism of iron-based NPs at the molecular level. In addition to their negative effects, ROS also play a significant positive role in dormancy release, seed germination signaling, protection against pathogens, and regulation of internal cellular machinery in response to external environmental dynamics. There is a specific "oxidative window" that allows cellular events to unfold in sequential order for seed germination if ROS are maintained within a particular range [90].

Moreover, it has been shown [91] that nanomaterials promote seed germination by forming nanopores in seed coats, introducing reactive oxygen species (ROS), increasing enzyme activity at starch-degrading sites, and introducing ROS to the seed coat.

Therefore, as bioactivity of GC–HA1 did not differ from that of GC–HA10 though the latter released significantly more ferrous ions, an acquisition of iron by seedlings seems not to be important from this point of view. In addition, extra-data on iron beneficial effect on seed germination are needed. On the other hand, comparing EDS and phytoassay data, one can conclude on similarity of GC–HA1 and GC–HA10 in terms of zeta-potential dependence on pH. Data presented in Fig. 6a show higher colloidal stability of nanoparticles modified with HA at pH 6–7 as compared to GC. Besides, additional steric stabilization of GC–HA1 and GC–HA10 NPs as compared to GC can be expected. So, overall, studied GC–HA1 and GC–HA10 demonstrated similar bioactivity and colloidal stability. As for the other properties (XRD, SEM, Moessbauer, etc.) GC–HA1 and GC–HA10 differed one from another. Therefore, it is most logical to look for an explanation of the observed biological activity in the colloidal properties of the nanoparticles under study. Higher stability of nanoparticles with HA at pH 6–7 can be considered as a leading reason of their more pronounced biological activity. A further study of the synthetized NPs' aggregation and ROS generation and their relationship to biological activity should be proposed.

Conclusions

We present the synthesis and characterization of goethite (G) nanoparticles intercalated in coal (GC) and modified by humic acids (HA) to enhance their bioactivity towards *Sinapis alba*. The synthesized GC was identified and characterized by scanning electron microscopy, X-ray diffraction, Mössbauer spectroscopy, N_2 adsorption–desorption BET specific surface area, zeta potential, release of iron ions, and phytoassay with higher plants.

The primary phase of the goethite structure was identified by X-ray diffraction in both the GC and goethite–humic acids (GC–HA) complexes. Mössbauer spectroscopy analysis revealed a mixture of Fe^{2+}-doped GC, possibly due to the redox potential of HA. The intercalation of GC in the coal matrix increased the specific surface area of GC, facilitating HA sorption. In addition, HA was found to promote plant growth stimulation due to colloidal stability of hybrid nanoparticles.

Compared to GC, the release of Fe^{3+} and Fe^{2+} from GC–HA was prolonged and more time-dependent. The revealed ferrous ion release from GC–HA10 can be considered as a promising result in terms of iron nanofertilizers production.

Abbreviations

G	Goethite
NPs	Nanoparticles
GC	Goethite nanoparticles intercalated in coal
HA	Humic acids
SEM	Scanning electron microscopy
BET	Brunauer–Emmett–Teller model
GC–HA	Complex of GC with humic acids
HS	Humic substances
S. alba	*Sinapis alba*
DI	Deionized water
GC–HA1 and GC–HA10	Samples of GC–HA complexes, where index indicates the HA concentration (in g) in complex
XRD	X-ray diffraction
BJH	Barrett–Joyner–Halenda model
SEC	Size exclusion chromatography
CV	Coefficient of variation
Kp	Polydispersity index
SSA	Specific surface area
ROS	Reactive oxygen species
nZVI	Nano-zero valent iron

Author contributions
Conceptualization, AM and KK; methodology, LB. and KK; software, AD and RZh; validation, VT and AM; formal analysis, DP; investigation, RZh, AD, DP, DS and LB; resources, VT and NT; writing—original draft preparation, KK and LB; writing—review and editing, KK, LB, VT, NT; supervision, KK and VT. All authors read and approved the final manuscript.

Zharkynbaeva *et al. Chem. Biol. Technol. Agric.*   (2024) 11:14

Page 15 of 17

Declarations

Ethics approval and consent to participate
Not applicable.

Consent for publication
Not applicable.

Competing interests
The authors declare that they have no competing interests.

Author details
[1]Osh State University, 723500 Osh, Kyrgyz Republic. [2]Moscow Aviation Institute (National Research University), Moscow 125993, Russia. [3]Federal Research Center of Problems of Chemical Physics and Medicinal Chemistry, Russian Academy of Sciences, Chernogolovka 142432, Moscow Region, Russia. [4]Sklifosovsky Research Institute for Emergency Medicine, Moscow 129090, Russia. [5]Lomonosov Moscow State University, Moscow 119991, Russia.

References
1. Camprubi E, Jordan SF, Vasiliadou R, Lane N. Iron catalysis at the origin of life. IUBMB Life. 2017;69:373–81. https://doi.org/10.1002/iub.1632.
2. Zhang S, Du Q, Sun Y, Song J, Yang F, Tsang DCW. Fabrication of L-cysteine stabilized α-FeOOH nanocomposite on porous hydrophilic biochar as an effective adsorbent for Pb^{2+} removal. Sci Total Environ. 2020;720: 137415. https://doi.org/10.1016/j.scitotenv.2020.137415.
3. Combes JM, Manceau A, Calas G, Bottero JY. Formation of ferric oxides from aqueous solutions: a polyhedral approach by X-ray absorption spectroscopy: I. Hydrolysis and formation of ferric gels. Geochim Cosmochim Acta. 1989;53:583–94. https://doi.org/10.1016/0016-7037(89)90001-X.
4. Jolivet JP, Chanéac C, Tronc E. Iron oxide chemistry. From molecular clusters to extended solid networks. Chem Commun. 2004;5:477–83. https://doi.org/10.1039/b304532n.
5. Marschner P, Rengel Z. Chapter 12: Nutrient availability in soils. In Marschner's mineral nutrition in higher plants, 3rd ed.; London: Academic; 2012. p. 315–330.
6. List of authorised organic chelating agents for micro-nutrients pursuant to Annex I, paragraph E.3.1. of Regulation (EC) N° 2003/2003 relating to fertilizers. 2003.
7. Inaba S, Takenaka C. Effects of dissolved organic matter on toxicity and bioavailability of copper for lettuce sprouts. Environ Int. 2005;31:603–8. https://doi.org/10.1016/j.envint.2004.10.017.
8. Imbufe AU, Patti AF, Burrow D, Surapaneni A, Jackson WR, Milner AD. Effects of potassium humate on aggregate stability of two soils from Victoria. Australia Geoderma. 2005;125:321–30. https://doi.org/10.1016/j.geoderma.2004.09.006.
9. John B, Yamashita T, Ludwig B, Flessa H. Storage of organic carbon in aggregate and density fractions of silty soils under different types of land use. Geoderma. 2005;128:63–79. https://doi.org/10.1016/j.geoderma.2004.12.013.
10. Devevre OC, Horwath WR. Stabilization of fertilizer nitrogen-15 into humic substances in aerobic vs. waterlogged soil following straw incorporation. Soil Sci Soc Am J. 2001;65:499–510.
11. García-Mina JM, Antolín MC, Sanchez-Diaz M. Metal-humic complexes and plant micronutrient uptake: a study based on different plant species cultivated in diverse soil types. Plant Soil. 2004;258:57–68. https://doi.org/10.1023/B:PLSO.0000016509.56780.40.
12. Agbenin JO, Olojo LA. Competitive adsorption of copper and zinc by a Bt horizon of a savanna Alfisol as affected by pH and selective removal of hydrous oxides and organic matter. Geoderma. 2004;119:85–95. https://doi.org/10.1016/S0016-7061(03)00242-8.
13. Khwaja AR, Bloom PR, Brezonik PL. Binding constants of divalent mercury [Hg^{2+}] in soil humic acids and soil organic matter. Environ Sci Technol. 2006;40:844–9. https://doi.org/10.1021/es051085c.
14. Pegoraro RF, Silva IR, Novais RF, Mendonca ES, Alvarez VH, Nunes FN, Fonseca FM, Smyth TJ. Diffusive flux of cationic micronutrients in two Oxisols as affected by low-molecular-weight organic acids and covercrop residue. J Plant Nutr Soil Sci. 2005;168:334–41. https://doi.org/10.1002/jpln.200421455.
15. Senesi N, Calderoni G. Structural and chemical characterization of copper, iron and manganese complexes formed by paleosol humic acids. Org Geochem. 1988;13:1145–52. https://doi.org/10.1016/0146-6380(88)90300-2.
16. Illes E, Tombacz E. The effect of humic acid adsorption on pH-dependent surface charging and aggregation of magnetite nanoparticles. J Colloid Interface Sci. 2006;295:115–23. https://doi.org/10.1016/j.jcis.2005.08.003.
17. Cesco S, Roemheld V, Varanini Z, Pinton R. Solubilization of iron by water-extractable humic substances. J Plant Nutr Soil Sci. 2000;163:285–90. https://doi.org/10.1002/1522-2624(200006)163:3%3c285::AID-JPLN285%3e3.0.CO;2-Z.
18. Kulikova NA, Perminova IV, Badun GA, Chernysheva MG, Koroleva OV, Tsvetkova EA. Estimation of uptake of humic substances from different sources by *Escherichia coli* cells under optimum and salt stress conditions by use of tritium-labeled humic materials. Appl Environ Microbiol. 2010;76:6223–30. https://doi.org/10.1128/AEM.00905-10.
19. Moura OVT, Berbara RLL, Torchia DFO, Silva HFO, Castro TAT, Tavarez OCH, Rodrigues NF, Santos LA, Garcia AC. Humic foliar application as sustainable technology for improving the growth, yield, and abiotic stress protection of agricultural crops. A review. J Saudi Soc Agric Sci. 2023. https://doi.org/10.1016/j.jssas.2023.05.001.
20. Herjsted LN. Process for preparing preferred iron humates. St. Louis Mo: Kemiron; 1991.
21. Zhilin DM, Schmitt-Kopplin P, Perminova IV. Reduction of Cr(VI) by peat and coal humic substance. Environ Chem Lett. 2004;2:141–5. https://doi.org/10.1007/s10311-004-0085-4.
22. Bar-Ness E, Chen Y. Manure and peat based iron-organo complexes. Plant Soil. 1991;130:35–43. https://doi.org/10.1007/BF00011853.
23. Pinton R, Cesco S, Santi S, Agnolon F, Varanini Z. Water-extractable humic substances enhance iron deficiency responses by Fe-deficient cucumber plants. Plant Soil. 1999;210:145–57. https://doi.org/10.1023/A:1004329513498.
24. Lobartini JC, Orioli GA. Absorption of iron Fe-humate in nutrient solutions by plants. Plant Soil. 1988;106:153–7. https://doi.org/10.1007/BF02371209.
25. Aguirre E, Lemenager D, Bacaicoa E, Fuentes M, Baigorri R, Zamarreno AM, Garcıa-Mina JM. The root application of a purified leonardite humic acid modifies the transcriptional regulation of the main physiological root 155 responses to Fe deficiency in Fe-sufficient cucumber plants. Plant Physiol Biochem. 2009;47:215–23. https://doi.org/10.1016/j.plaphy.2008.11.013.
26. Chen Y, Clapp CE, Magen H. Mechanisms of plant growth stimulation by humic substances: the role of organo-iron complexes. Soil Sci Plant Nutr. 2004;50:1089–95. https://doi.org/10.1080/00380768.2004.10408579.
27. Yao Y, Gao B, Fang J, Zhang M, Chen H, Zhou Y, Creamer AE, Sun Y, Yang L. Characterization and environmental applications of clay–biochar composites. Chem Eng Sci. 2014;242:136–43. https://doi.org/10.1016/j.cej.2013.12.062.
28. Goldberg S, Forster HS, Godfrey CL. Molybdenum adsorption on oxides, clay minerals, and soils. Soil Sci Soc Am J. 1996;60:425. https://doi.org/10.2136/sssaj1996.03615995006000020013x.
29. Vithanage M, Chandrajith R, Bandara A, Weerasooriya R. Mechanistic modeling of arsenic retention on natural red earth in simulated environmental systems. J Colloid Interface Sci. 2006;294:265–72. https://doi.org/10.1016/j.jcis.2005.07.026.
30. Rajapaksha AU, Chen SS, Tsang DCW, Zhang M, Vithanage M, Mandal S, Gao B, Bolan NS, Ok YS. Engineered/designer biochar for contaminant removal/immobilization from soil and water: potential and implication of

Zharkynbaeva *et al. Chem. Biol. Technol. Agric.*   (2024) 11:14

Page 16 of 17

biochar modification. Chemosphere. 2016;148:276–91. https://doi.org/10.1016/j.chemosphere.2016.01.043.

31. Atkinson CJ, Fitzgerald JD, Hipps NA. Potential mechanisms for achieving agricultural benefits from biochar application to temperate soils: a review. Plant Soil. 2010;337:1–18. https://doi.org/10.1007/s11104-010-0464-5.

32. Beesley L, Moreno-Jiménez E, Gomez-Eyles JL, Harris E, Robinson B, Sizmur T. A review of biochars' potential role in the remediation, revegetation and restoration of contaminated soils. Environ Pollut. 2011;159:3269–82. https://doi.org/10.1016/j.envpol.2011.07.023.

33. Lehmann J, Rillig MC, Thies J, Masiello CA, Hockaday WC, Crowley D. Biochar effects on soil biota—a review. Soil Biol Biochem. 2011;43:1812–36. https://doi.org/10.1016/j.soilbio.2011.04.022.

34. Olk DC, Yakimenko OS, Kussow WR, Dinnes DL. Can humic products become mainstream amendments for improving crop production? Third International Conference of CIS IHSS on Humic Innovative Technologies Tenth International Conference daRostim «Humic Substances and Other Biologically Active Compounds in Agriculture» HIT-daRostim-2014, Lomonosov Moscow State University, Moscow, Russia, November 19 - 23, 2014, P.291–292.

35. Cheng G, Niu Z, Zhang C, Zhang X, Li X. Extraction of humic acid from lignite by koh-hydrothermal method. Appl Sci. 2019;9:1356. https://doi.org/10.3390/app9071356.

36. Hiemstra T, Van Riemsdijk WH, Bolt GH. Multisite proton adsorption modeling at the solid/solution interface of (hydr)oxides: a new approach. J Colloid Interface Sci. 1989;133:91–104. https://doi.org/10.1016/0021-9797(89)90284-1.

37. De La Vega JC, Elischer P, Schneider T, Häfeli UO. Uniform polymer microspheres: monodispersity criteria, methods of formation and applications. Nanomedicine. 2013;8:265–85. https://doi.org/10.2217/nnm.12.210.

38. Inbar Y, Hadar Y, Chen Y. Characterization of humic substances formed during the composting of solid wastes from wineries. Sci Total Environ. 1992;113:35–48. https://doi.org/10.1016/0048-9697(92)90015-k.

39. Perdue EM. Acidic functional groups of humic substances. In: Aiken GR, McKnight DM, Wershaw RL, MacCarthy P, editors. Humic substances in soil, sediment and water. New York: Wiley Interscience; 1985. p. 493–525.

40. Perminova IV, Frimmel FH, Kovalevskii DV, Abbt-Braun G, Kudryavtsev AV, Hesse S. Development of a predictive model for calculation of molecular weight of humic substances. Water Res. 1998;32:872–81. https://doi.org/10.1016/S0043-1354(97)00283-2.

41. Tang S, Chang Y, Shen W, Lee HK. Selective extraction by dissolvable (nitriloacetic acid-nickel)-layered double hydroxide coupled with reaction with potassium thiocyanate for sensitive detection of iron(III). Talanta. 2016;154:416–22. https://doi.org/10.1016/j.talanta.2016.03.096.

42. Tripathi AD, Gupta KA, Malik Sh. Iron determination by colorimetric method using o-phenanthroline. BPAS. 2019;38:171–5. https://doi.org/10.5958/2320-320X.2019.00018.9.

43. Prudnikova EV, Neaman A, Terekhova VA, Karpukhin MM, Vorobeichik EL, Smorkalov IA, Dovletyarova EA, Navarro-Villarroel C, Ginocchio R, Peñaloza P. Root elongation method for the quality assessment of metal-polluted soils: whole soil or soil-water extract? J Soil Sci Plant Nutr. 2020;20:2294–303. https://doi.org/10.1007/s42729-020-00295-x.

44. Nikolaeva OV, Terekhova VA. Improvement of laboratory phytotest for the ecological evaluation of soils. Eurasian Soil Sci. 2017;50:1105–14. https://doi.org/10.1134/S1064229317090058.

45. Hazemann JL, Bérar JF, Manceau A. Rietveld studies of the aluminium-iron substitution in synthetic goethite. Mater Sci Forum. 1991;79–82:821–6. https://doi.org/10.4028/www.scientific.net/msf.79-82.821.

46. Wang J, Sun J, Sun Q, Chen Q. One-step hydrothermal process to prepare highly crystalline Fe_3O_4 nanoparticles with improved magnetic properties. Mater Res Bull. 2003;38:1113–8. https://doi.org/10.1016/s0025-5408(03)00129-6.

47. Piccolo A. The supramolecular structure of HS. Soil Sci. 2001;166:810–32.

48. Sutton R, Sposito G. Molecular structure in soil humic substances: The new view. Environ Sci Technol. 2005;39:9009–15. https://doi.org/10.1021/es050778q.

49. Lv J, Zhang S, Wang S, Luo L, Cao D, Christie P. Molecular-scale investigation with ESI-FT-ICR-MS on Fractionation of dissolved organic matter induced by adsorption on iron oxyhydroxides. Environ Sci Technol. 2016;50:2328–36. https://doi.org/10.1021/acs.est.5b04996.

50. Valeev D, Pankratov D, Shoppert A, Sokolov A, Kasikov A, Mikhailova A, Salazar-Concha C, Rodionov I. Mechanism and kinetics of iron extraction

from high silica boehmite–kaolinite bauxite by hydrochloric acid leaching. Trans Nonferrous Met Soc China. 2021;31:3128–49. https://doi.org/10.1016/S1003-6326(21)65721-7.

51. Shoppert A, Valeev D, Diallo MM, Loginova I, Beavogui MC, Rakhmonov A, Ovchenkov Y, Pankratov D. High-iron bauxite residue (red mud) valorization using hydrochemical conversion of goethite to magnetite. Materials. 2022;15:8423. https://doi.org/10.3390/ma15238423.

52. Pankratov DA, Anuchina MM. Nature-inspired synthesis of magnetic non-stoichiometric Fe_3O_4 nanoparticles by oxidative in situ method in a humic medium. Mater Chem Phys. 2019;231:216–24. https://doi.org/10.1016/j.matchemphys.2019.04.022.

53. Pankratov DA, Anuchina MM, Spiridonov FM, Krivtsov GG. $Fe_{3 − δ}O_4$ nanoparticles synthesized in the presence of natural polyelectrolytes. Crystallogr Rep. 2020;65:393–7. https://doi.org/10.1134/s1063774520030244.

54. Pankratov DA. Mössbauer study of oxo derivatives of iron in the Fe_2O_3-Na_2O_2 system. Inorg Mater. 2013;50:82–9. https://doi.org/10.1134/s0020168514010154.

55. Pankratov DA, Anuchina MM, Konstantinov AI, Perminova IV. Analyzing the dynamics of interaction between humic coal substances and metallic iron. Russ J Phys Chem A. 2019;93:1235–44. https://doi.org/10.1134/s0036024419070203.

56. Pankratov DA, Anuchina MM. Role of humic substances in the formation of nanosized particles of iron corrosion products. Russ J Phys Chem A. 2017;91:233–9. https://doi.org/10.1134/s0036024417020224.

57. Skogerboe RK, Wilson SA. Reduction of ionic species by fulvic acid. Anal Chem. 1981;53:228–32. https://doi.org/10.1021/ac00225a023.

58. Struyk Z, Sposito G. Redox properties of standard humic acids. Geoderma. 2001;102:329–46. https://doi.org/10.1016/s0016-7061(01)00040-4.

59. Nevin KP, Lovley DR. Mechanisms for Fe(III) oxide reduction in sedimentary environments. Geomicrobiol J. 2002;19:141–59. https://doi.org/10.1080/01490450252864253.

60. Roden EE, Kappler A, Bauer I, Jiang J, Paul A, Stoesser R, Konishi H, Xu H. Extracellular electron transfer through microbial reduction of solid-phase humic substances. Nat Geosci. 2010. https://doi.org/10.1038/ngeo870.

61. Rakshit S, Uchimiya M, Sposito G. Iron(III) bioreduction in soil in the presence of added humic substances. Soil Sci Soc Am J. 2009;73:65–71. https://doi.org/10.2136/sssaj2007.0418.

62. Kosmulski M, Maczka E, Jartych E, Rosenholm JB. Synthesis and characterization of goethite and goethite–hematite composite: experimental study and literature survey. Adv Colloid Interface Sci. 2003;103:57–76. https://doi.org/10.1016/S0001-8686(02)00083-0.

63. Steinegger A, Wolfbeis OS, Borisov SM. Optical sensing and imaging of pH values: spectroscopies, materials, and applications. Chem Rev. 2020;120:12357–489. https://doi.org/10.1021/acs.chemrev.0c00451.

64. Ghosh K, Schnitzer M. Macromolecular structures of humic substances. Soil Sci. 1980;129:266–76. https://doi.org/10.1097/00010694-19800 5000-00002.

65. De Melo BAG, Motta FL, Santana MHA. The interactions between humic acids and pluronic F127 produce nanoparticles useful for pharmaceutical applications. J Nanopart Res. 2015. https://doi.org/10.1007/s11051-015-3204-1.

66. Fukushima M, Tanaka S, Hasebe K, Taga M, Nakamura H. Interpretation of the acid-base equilibrium of humic acid by a continuous pK distribution and electrostatic model. Anal Chim Acta. 1995;302:365–73. https://doi.org/10.1016/0003-2670(94)00471-w.

67. Atalay YB, Carbonaro RF, Di Toro DM. Distribution of proton dissociation constants for model humic and fulvic acid molecules. Environ Sci Technol. 2009;43:3626–31. https://doi.org/10.1021/es803057r.

68. Klučáková M, Kolajová R. Dissociation ability of humic acids: Spectroscopic determination of pKa and comparison with multi-step mechanism. React Funct Polym. 2014;78:1–6. https://doi.org/10.1016/j.reactfunctpolym.2014.02.005.

69. Siéliéchi J-M, Lartiges BS, Kayem GJ, Hupont S, Frochot C, Thieme J, Ghanbaja J, d'Espinose de la Caillerie JB, Barrès O, Kamga R, Levitz P, Michot LJ. Changes in humic acid conformation during coagulation with ferric chloride: Implications for drinking water treatment. Water Res. 2008;42:2111–23. https://doi.org/10.1016/j.watres.2007.11.017.

70. Kicheeva AG, Sushko ES, Bondarenko LS, Kydralieva KA, Pankratov DA, Tropskaya NS, Dzeranov AA, Dzhardimalieva GI, Zarrelli M, Kudryasheva NS. Functionalized magnetite nanoparticles: characterization, bioeffects,

Zharkynbaeva *et al. Chem. Biol. Technol. Agric.*   (2024) 11:14

Page 17 of 17

and role of reactive oxygen species in unicellular and enzymatic systems. Int J Mol Sci. 2023;24:1133. https://doi.org/10.3390/ijms24021133.

71. Arancon NQ, Edwards CA, Lee S, Byrne R. Effects of humic acids from vermicomposts on plant growth. Eur J Soil Biol. 2006;42:65–9. https://doi.org/10.1016/j.ejsobi.2006.06.004.

72. Dzeranov A, Bondarenko L, Pankratov D, Prokofev M, Dzhardimalieva G, Jorobekova S, Tropskaya N, Telegina L, Kydralieva K. Iron oxides nanoparticles as components of ferroptosis-inducing systems: screening of potential candidates. Magnetochemistry. 2023. https://doi.org/10.3390/magnetochemistry9010003.

73. Handler RM, Beard BL, Johnson CM, Scherer MM. Atom exchange between aqueous Fe(II) and goethite: An Fe isotope tracer study. Environ Sci Technol. 2009;43:1102–7. https://doi.org/10.1021/es802402m.

74. Ersoy B, Tosun I, Günay A, Dikmen S. Turbidity removal from wastewaters of natural stone processing by coagulation/flocculation methods. CLEAN - Soil, Air, Water. 2009;37:225–32. https://doi.org/10.1002/clen.200800209.

75. Parfitt R, Parfitt RL, Fraser AR, Farmer VC. Adsorption on hydrous oxides. III. Fulvic acid and humic acid on goethite, gibbsite and imogolite. Eur J Soil Sci. 1977;28:289–96. https://doi.org/10.1111/j.1365-2389.1977.tb02237.x.

76. Noyes AA, Whitney WR. The rate of solution of solid substances in their own solutions. J Am Chem Soc. 1897;19:930–4. https://doi.org/10.1021/ja02086a003.

77. Mihranyan A, Strømme M. Solubility of fractal nanoparticles. Surf Sci. 2007;601:315–9. https://doi.org/10.1016/j.susc.2006.09.037.

78. Schulte EE. Fertilizer sources of iron. Understanding Plant Nutrients. 2004;9:2.

79. Briat JF. Le fer du sol aux produits végétaux. Bull Acad Natl Med. 2005;189:1609–21. https://doi.org/10.1016/s0001-4079(19)33419-3.

80. Weng L, Van Riemsdijk WH, Hiemstra T. Cu^{2+} and Ca^{2+} adsorption to goethite in the presence of fulvic acids. Geochim Cosmochim Acta. 2008;72:5857–70. https://doi.org/10.1016/j.gca.2008.09.015.

81. Lindsay WL. Chemical equilibria in soils. New York: Wiley Interscience; 1979. p. 449.

82. Cline GR, Powell PE, Szaniszlo PJ, Reid CPP. Comparison of the abilities of hydroxamic acid, synthetic and other natural organic acids to chelate iron and other ions in nutrient solution. Soil Sci Soc Am J. 1982;46:1158–64. https://doi.org/10.2136/sssaj1982.03615995004600060008x.

83. Stevenson FJ. Humus chemistry: genesis, composition, reactions. New York: Wiley Interscience; 1982. p. 465.

84. Bondarenko L, Kahru A, Terekhova V, Dzhardimalieva G, Uchanov P, Kydralieva K. Effects of humic acids on the ecotoxicity of Fe_3O_4 nanoparticles and Fe-ions: Impact of oxidation and aging. Nanomater. 2020;10:2011. https://doi.org/10.3390/nano10102011.

85. Von Moos N, Slaveykova VI. Oxidative stress induced by inorganic nanoparticles in bacteria and aquatic microalgae—state of the art and knowledge gaps. Nanotoxicology. 2013;8:605–30. https://doi.org/10.3109/17435390.2013.809810.

86. Li H, Zhou Q, Wu Y, Fu J, Wang T, Jiang G. Effects of waterborne nano-iron on medaka (Oryzias latipes): antioxidant enzymatic activity, lipid peroxidation and histopathology. Ecotoxicol Environ Saf. 2009;72:684–92. https://doi.org/10.1016/j.ecoenv.2008.09.027.

87. Che P-J, Tan S-W, Wu W-L. Stabilization or oxidation of nanoscale zerovalent iron at environmentally relevant exposure changes bioavailability and toxicity in medaka fish. Environ Sci Technol. 2012;46:8431–9. https://doi.org/10.1021/es3006783.

88. Chen P-J, Wu W-L, Wu K-W. The zerovalent iron nanoparticle causes higher developmental toxicity than its oxidation products in early life stages of medaka fish. Water Res. 2013;47:3899–909. https://doi.org/10.1016/j.watres.2012.12.043.

89. Chaithawiwat K, Vangnai A, McEvoy JM, Pruess B, Krajangpan S, Khan E. Role of oxidative stress in inactivation of Escherichia coli BW25113 by nanoscale zero-valent iron. Sci Total Environ. 2016;565:857–62. https://doi.org/10.1016/j.scitotenv.2016.02.191.

90. Anand A, Kumari A, Thakur M, Koul A. Hydrogen peroxide signaling integrates with phytohormones during the germination of magnetoprimed tomato seeds. Sci Rep. 2019;9:8814. https://doi.org/10.1038/s41598-019-45102-5.

91. Shelar A, Nile SH, Singh AV, Rothenstein D, Bill J, Xiao J, Chaskar M, Kai G, Patil R. Recent advances in nano-enabled seed treatment strategies for sustainable agriculture: challenges, risk assessment, and future perspectives. Nano-Micro Lett. 2023;15:54. https://doi.org/10.1007/s40820-023-01025-5.

Publisher's Note